Animatronic Soft Robots by Additive Folding

S. Yim[1*], C. Sung[2], S. Miyashita[3], D. Rus[2], and S. Kim[4]

Abstract—This paper presents a new desktop fabrication concept called additive folding that creates animatronic soft robots with one-step assembly and built-in actuation. Additive folding is a new mechanism where 2D slices threaded by a string are accordion-folded and stacked into a 3D structure. The slices are articulated using flexure hinges that enable the folded structure to deform and move like creatures. We created a computational design algorithm that takes as input a desired 3D geometry, and that computes a 2D surface with built-in folds and placements for string-based actuators. This paper describes the entire process for designing the animatronic soft robot given a target 3D geometry, and demonstrates its soft and natural motions, highlighting the vision of desk-top fabrication technology and its potential applications in animatronics and robotics.

1. INTRODUCTION

We imagine a future when desktop fabrication of complex robotic systems is as easy and intuitive as printing on paper today. Personalized fabrication that takes place on the user's desktop has the potential to democratize and customize fabrication and manufacturing, allowing consumers to be much more involved in the production of their products. 3D printing, technically known as *additive manufacturing*, has enabled such on-demand digital fabrication of a wide variety of 3D physical objects from geometric models (Gibson et al., 2010), and created innovative applications in homes, hospitals, art, apparel, food and academic research. For example, people decorate their houses with 3D printed furniture (Micallef et al., 2015). Doctors can touch 3D models of body parts reconstructed from ultrasound images (Lipson et al., 2013) and build preoperative planning and test the protocol using prototyped simulators (Müller et al., 2003; Poukens et al., 2003). Dentists can fabricate and implant ceramic-made artificial teeth (Dawood et al., 2015). Large-scale 3D printing aims to create entire houses, apartments and even a lunar base (Davison et al., 2015; Perkins et al., 2015; Cesaretti et al., 2014). Pioneering scientists are fabricating not only different microelectronic devices but also personalized bionic implants, organs and even nerves (Morrison et al., 2015; Murphy et al., 2014; Kang et al., 2016; Jung et al., 2016). Multi-scale 3D printing is changing research paradigms and impacting everyday life.

3D printing also enables a design and fabrication revolution in robotics where smart machines can move, sense, compute, and communicate (MacCurdy et al., 2016). Current challenges for rapid-prototypable 3D robots include (i) a short manufacturing time (Tumbleston et al., 2015), (ii) the use of a wide variety of materials (Eckel et al., 2016; Ribeiro et al., 1998; Peng et al., 2015; Wang et al., 2016) and (iii) the ability to integrate electromechanical devices such as sensors (Yokota et al., 2015; Muth et al., 2014), actuators (Bartlett et al., 2015), batteries (Kim et al., 2015; Sun et al., 2013), controller units (Espalin et al., 2014), and programmable matter (Hawkes et al., 2010; Goldstein et al., 2005). In this paper, we develop a new concept called *additive folding*, in which 2D slices are chain-connected, accordion-folded, and stacked-up to create animatronic soft robots of desired 3D shapes. Our main contribution include:

S. Yim is with [1]Robotics and Media Institute, Korea Institute of Science and Technology, Seoul 02792, S. Korea (e-mail: sehyuky@kist.re.kr).
C. Sung and D. Rus are with [2]Computer Science and Artificial Intelligence Laboratory, Massachusetts Institute of Technology, Cambridge, MA 02139, USA.
S. Miyashita is with [3]University of York, Department of Electronic Engineering, Heslington, York, YO10 5DD, UK.
S. Kim is with [4]the Department of Mechanical Engineering, Massachusetts Institute of Technology, Cambridge, MA 02139.

- A new fabrication technique that structures and assembles compliant 2D materials into soft 3D robots of elaborate design.
- Computational algorithms for modeling and designing the fold patterns of 3D models.
- Experimental implementation of various animatronic motions using embedded flexible strings inside the robots.

This paper details the end-to-end implementation process with a miniature soft bunny robot as an example (Fig. 1), describing underlying physical principles regarding additive folding of elastic materials and the soft actuation mechanism with flexible strings. As the results show, its various motions and continuous body deformation using the interaction between muscle-like strings and the elastic bodies are soft and natural. Finally, we will discuss open issues and possible improvements, which are needed to expand additive folding to the future 3D fabrication technology as well as robotics.

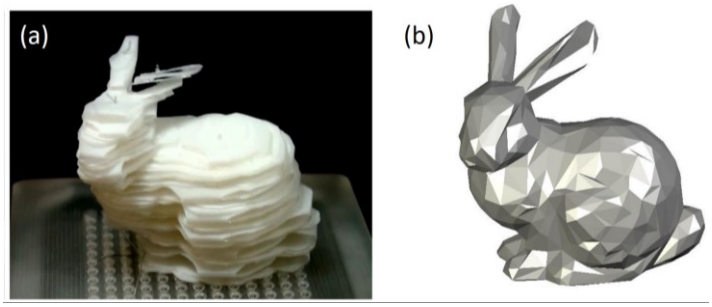

Fig. 1. (a) The animatronic soft bunny robot fabricated by additive folding and (b) its geometric model.

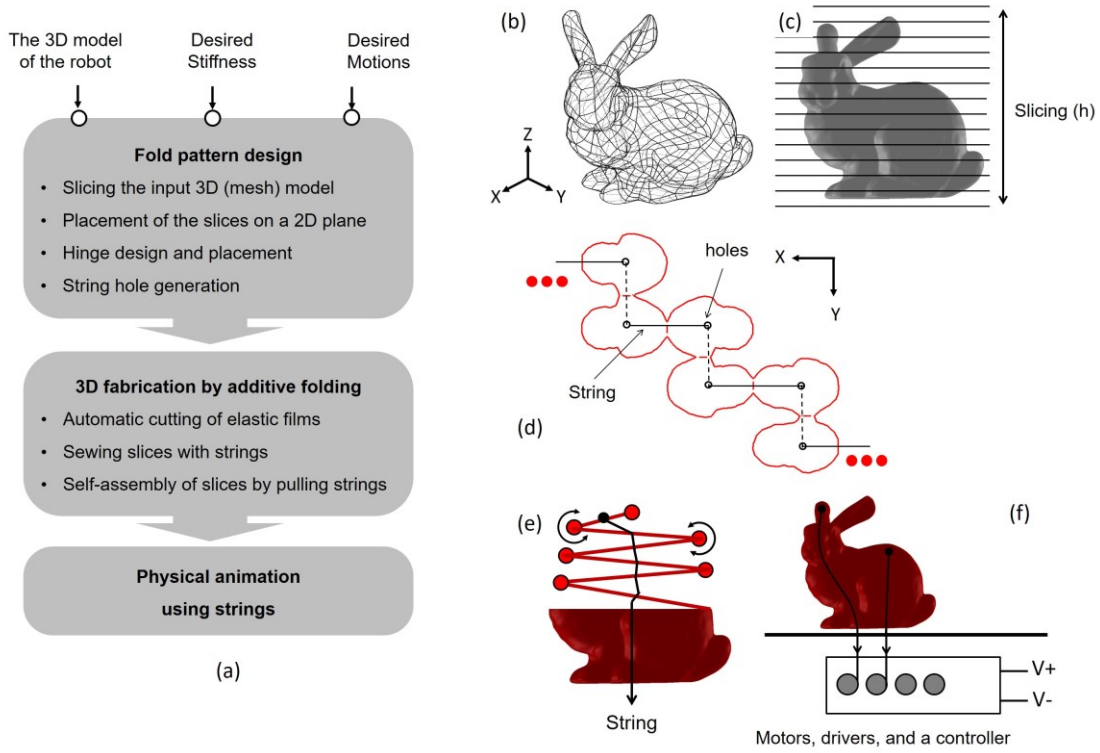

Fig. 2. The implementation scheme of an animatronic soft robot (e.g., a bunny model) by additive folding. (a) The flow diagram consisting of computational design, fabrication by additive folding and physical animation. (b) The input 3D mesh model. (c) Slicing the model into multiple layers. *h* is the resolution of the sliced model in the vertical direction. (d) Placing the slices onto a 2D plane and generating hinges and holes for strings. The designed fold pattern is manufactured by cutting elastic 2D materials (e.g., polyester films) with a desktop paper crafting machine. The articulated slices are threaded with strings, which become muscles routing each part of the robot. (e) Pulling the strings for assembling the 2D strip into the defined 3D model. (f) Animating the fabricated 3D structure by actuating the extended parts of the strings under the stage. See the multimedia extension 1.

2. Computational Design

Animatronic soft robots are created by three major steps: computational design, desk-top fabrication and physical animation (Fig. 2). This section presents how the developed algorithm generates a 2D fold pattern consisting of slices, hinges and string holes from a 3D virtual model of the robot.

2.1. Slice Arrangement

First, the 3D mesh model (Fig. 2(b)) is sliced along a given axis. The resolution of slicing corresponds to the thickness of the sheet material and the gap distance between layers, which a user can set (Fig. 2(c)). Small gaps produce higher resolution robots made of a larger number of layers while larger gaps allow a wide motion range when actuated. If the model geometry has a local maximum (e.g., the back of the bunny model), some slices have multiple polygons. In order to simplify the pattern design process, the patterns of these parts are individually designed, and then merged with the main part one.

After making a model geometry where every slice has a single polygon, the slices are placed adjacent on a plane as if an accordion-folded 3D model is unfolded from the base (Fig. 2(d)). There are two ways to arrange the slices. In the first option,

they are straightly arranged in the x direction. As shown in Fig, 3(a), the algorithm detects the max x coordinate of polygon points of the bottom layer (S_0, $z = 0$) and the upper layer (S_1, $z = h$); $u_0^1 = \max(u_0, u_1)$ where h is the gap distance between layers, u_0 and u_1 are respectively the x coordinates of rightmost points of the two layers. Assuming that the accordion-folded 3D model rolls to the right and the upper layer is unfolded about the first crease ($x = u_0^1$), each polygon point of all slices except for the bottom layer is converted as $[x_0\ y_0\ z_0]^T$ and $[x_1\ y_1\ z_1]^T$ in Fig. 3(b). The general form of this transformation is

$$\begin{bmatrix} x_{k+1} \\ y_{k+1} \\ z_{k+1} \end{bmatrix} = \begin{bmatrix} -1 & 0 & 0 \\ 0 & 1 & 0 \\ 0 & 0 & -1 \end{bmatrix} \begin{bmatrix} x_k \\ y_k \\ z_k \end{bmatrix} + \begin{bmatrix} 2u_k^{k+1} \\ 0 \\ (-1)^k h \end{bmatrix} \tag{1}$$

and expressed as $P_{k+1} = MP_k + F_k^{k+1}$ where P_k and P_{k+1} respectively mean the 3D coordinate of a polygon point before and after unfolding the slices about $x = u_k^{k+1}$, k means the total number of completely unfolded slices (except for the base one), M is the constant 3-by-3 matrix, and the components of F, u_k^{k+1} and $(-1)^k h$, are updated after every unfolding. We define this transformation $P_{k+1} = U_k^{k+1}(P_k)$, and apply to each polygon point of all slices while $k = 0$ to n_{max}-1. As a result, all slices are layered one-by-one on the plane ($z = 0$) in the x-direction. The key part of this process is declared in algorithm 1. This arrangement method is useful to express a 3D robot of delicate and dense geometry because the resulting folded model has hinges on its left and right sides.

Alternatively, the slices could be placed like a staircase in order to have hinges at four directions when folded (Fig. 2(d)). These hinges act as pillars supporting the structure in four directions respectively. Thus, the 3D structure is more stable than the result of a straight fold pattern. Also, the robot is agile and has large motion ranges because the hinges generate shape restoring forces in all directions. In this method, Eq. (1) and (2) are alternately applied to the slices to unfold the slices in the x and y directions.

$$\begin{bmatrix} x_{k+1} \\ y_{k+1} \\ z_{k+1} \end{bmatrix} = \begin{bmatrix} 1 & 0 & 0 \\ 0 & -1 & 0 \\ 0 & 0 & -1 \end{bmatrix} \begin{bmatrix} x_k \\ y_k \\ z_k \end{bmatrix} + \begin{bmatrix} 0 \\ 2u_k^{k+1} \\ (-1)^k h \end{bmatrix} \tag{2}$$

By attaching slices along the limited direction, in both arrangement methods, a single fold pattern will not double back and self-intersect at any other location. When merging multiple crease patterns together, however, they can conflict each other. In that case, users can change unfolding directions of the conflicting slices to secure the margin between them.

Algorithm 1: SLICES($\mathbb{M}$, n_{max}, h)

Input: A mesh $\mathbb{M}_3$, total number of layers n_{max}, slice height h
Output: A 2D fold pattern of slices $\mathbb{F}$

```
1  for m = 0 to n_max do
2      z ← mh;
3      S_m ← slice of M at z;
4      Add polygon points in S_m to P
5  end
6  F ← S_0; B ← S_1;
7  for k = 0 to n_max -1
8      u_k^{k+1} ← max x coordinate of F and B;
9      foreach polygon point P_i in P do
10         if (z value of P_i is not 0) then
11             P_i ← U_k^{k+1} P_i;
12             Update P_i in P;
13             if (z value of P_i = 0)
14                 Add P_i to F;
15             end
16             if (z value of P_i = h or -h)
17                 Add P_i to B;
18             end
19         end
20     end
21 end
```

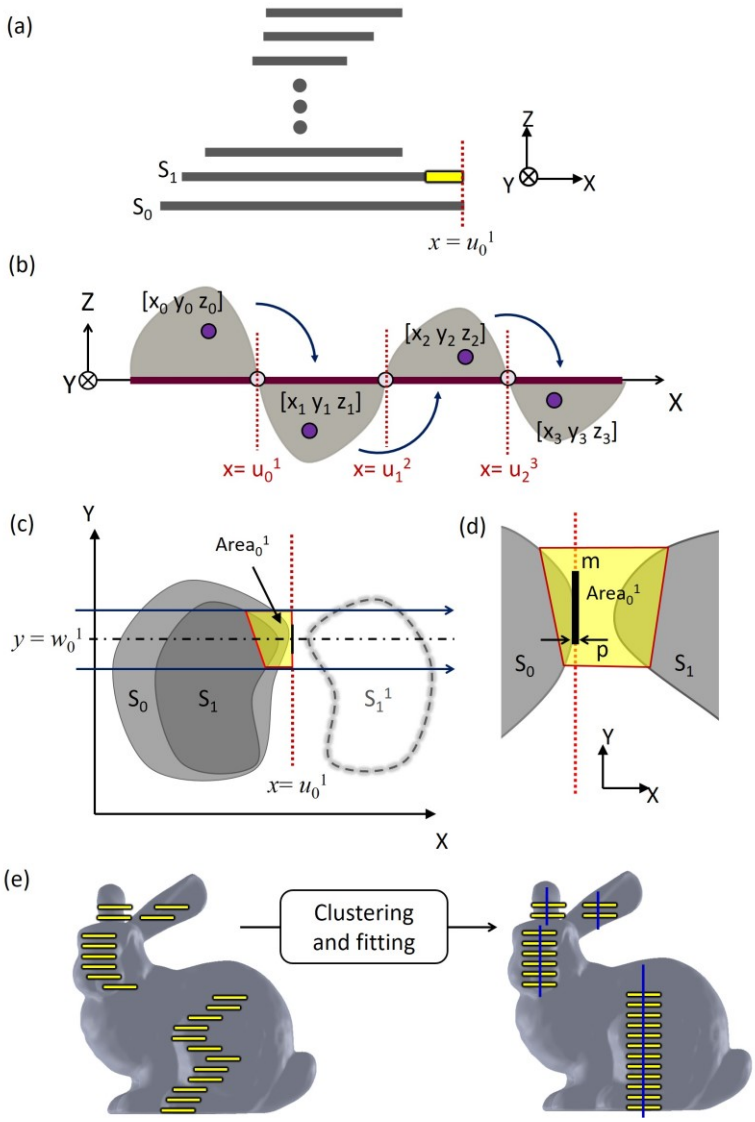

Fig. 3. Computational design of the fold pattern including slices and hinges. (a) Detecting the right most point of the two layers, and making the foldable line ($x = u_0^1$). (b) The purple points indicate the same polygon points before and after each unfolding. Their 3D coordinates are sequentially transformed by Eq. (1) as if an accordion-folded 3D model is rolled to the right side (+x direction). The white points and the red lines respectively present the foldable lines (i.e., $x = u_k^{k+1}$) and completely unfolded slices on the XY plane. (c) The top-view shows an example of how the hinge is generated between S_0 and S_1. The navy-colored lines indicate the two side lines of the hinge to minimize $Area_0^1$, the yellow area surrounded by the slices and these lines. (d) Design variables of the hinge between slices that have two bridges at the sides. (e) The hinges of all layers are initially set in 3D by the optimization process, and then adjusted to be on the vertical lines using cluster analysis for making the stacked hinges support the 3D structure.

2.2. Flexure Hinge Design

The second input of the pattern design function is the desired stiffness of the robot. We designed a rectangular hinge that has a slit at the center and two bridges connecting neighboring slices together. This slit functions to accurately fold slices during the assembly process. Regulating the bridge width m between slices (Fig. 3(d)), we can set the overall compliance of the robot in the stacking direction. Assuming that the completely folded hinges are vertical springs, the compliance of the bridge part is modeled with

$$C_z \propto \frac{r_0}{Emt^3} \tag{3}$$

where r_0 is the bending radius of completely folded hinges (normally, this is approximately one half of the gap distance h), E is the Young's modulus of the material and t is the thickness of the thin film. The net compliance of the model consisting of serially connected springs is roughly estimated using

$$C_{net} = \sum_{i=0}^{top} C_{z,i} \tag{4}$$

After fixing the parameters, the design algorithm determines locations of the hinges, following two steps. First, it finds the optimal position of each hinge that minimizes the increased area between slices (i.e., $\min(Area_0^1)$ in Fig. 3(c)); this area is computed using the intersection points of the polygons and the hinge lines in 3D, and the equivalent area is shown in Fig. 3(d). This process is for minimizing the shape change in 3D model geometry due to hinges. Next, the positions of the hinges are adjusted using clustering and (centroid) fitting (Fig. 3(e)). This rearrangement process enhances the stability of the 3D structure when the slices are stacked up by pulling flexible strings. The key part of hinge design process is detailed in Algorithm 2.

Algorithm 2: HINGES($\mathbb{S}$, n_{max}, d, c_L, c_R)

Input: $\mathbb{S}$ (slices S_k where $k = 0$ to n_{max}), hinge width d, the number of clusters c_L and c_R for left and right hinges
Output: 3D coordinates of polygon points in the slice Q_k where $k = 0$ to n_{max}

for $k = 0$ **to** n_{max} -1 **do** // INITIAL ARRANGEMENT
  if (k is even number) **then**
    $u_k^{k+1} \leftarrow$ max x coordinate of S_k and S_{k+1};
  else
    $u_k^{k+1} \leftarrow$ min x coordinate of S_k and S_{k+1};
  end
  $w_k^{k+1} \leftarrow$ optimized w to minimize $Area_k^{k+1}$; //Function AREA(u_k^{k+1}, S_k, S_{k+1}, d, w);
  Add w_k^{k+1} to $\mathbb{H}$;
end
$\mathbb{H}_c \leftarrow$ slice index, cluster index and centroid of $\mathbb{H}$; //Function CLUSTER($\mathbb{H}$, c_L, c_R)
for $k = 0$ to n_{max} -1 **do** // REARRANGEMENT
  $v_k \leftarrow$ centroid of $\mathbb{H}_c(k)$;
  $P_k \leftarrow$ intersection points of $y = v_k^{k+1} \pm 0.5d$, $x = u_k^{k+1}$ and a polygon S_k;
  $R_k \leftarrow$ polygon points of S_k inside P_k removed;
  $Q_k \leftarrow R_k$ merged with P_k;
end

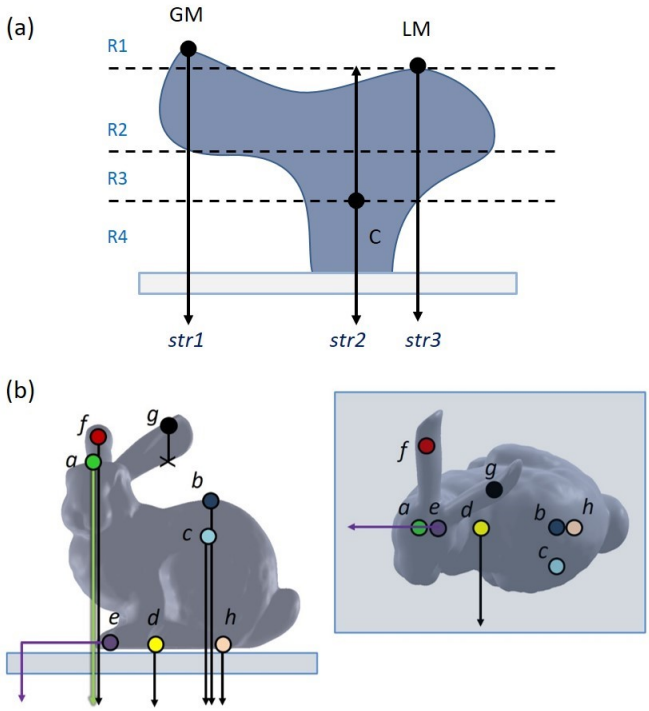

Fig. 4. Routing slices with strings. (a) The placement of the assembly strings to fold all layers of an arbitrary 3D model. The first string, str1, starts from the centroid of the top layer (e.g., global maximum) in the region R1, and the second string, *str*2, generates holes from the local minimum (LMN) as a new polygon is detected in the top layer of the region R2. R3 is still covered by *str*2. The third string, *str*3, is generated at the centroid of the top layer in the region R4 as the slice is not routed through by any of *str*1 or *str*2. Once a new string is generated, its hole is projected to all slices to route through all layers. (b) The side-view and the top-view of the bunny robot showing the paths of all strings. All layers are threaded by at least one of the four assembly strings *a, b, c, f*, and *g*. The strings *d, e*, and *h* generate its global motion in 2D such as translation and rotation. The string *g* for the left ear could be tied after additive folding.

2.3. String Routing Strategy

The final step of designing the fold pattern is to locate holes that strings are routed through. Each model has holes for two kinds of strings as follows, and the developed algorithm generates the strings using the 3D model first, and then converts the locations of string holes to the 2D fold pattern.

i) *Assembly and Local Actuation Strings*: these strings act as flexible skeletons for folding slices at the 3D assembly stage (detailed at Section 3), and later used for local actuation at the physical animation stage (detailed at Section 4). All slices should include at least one assembly string. Fig. 4(a) shows an example of how three assembly strings are generated in an arbitrary 3D model. First, the algorithm slices the 3D model from the top to the base. It generates a string hole at the centroid of the top layer, and then projects it onto the other layers in the 3D view (See the string str_1). While moving down to the base, if the projected sting hole goes outside the polygon or a new polygon is detected in slices (because of local maxima), new string holes are generated at the centroids of the polygons and projected to the upper and lower layers in the vertical direction (see *str*2 and *str*3 for these cases). In the case of the bunny model, four assembly strings for its upper body (including the head), the lower body (including the back), and two ears are produced. After the set of the holes is determined, their 3D coordinates are converted to 2D coordinates when unfolding the slices.

Algorithm 3: HOLES($\mathbb{S}$, n_{max})

Input: $\mathbb{S}$ (slices S_k where k = 0 to n_{max}), total number of layers n_{max}
Output: x and y coordinates of holes $\mathbb{A}$

```
Add Centroid of the top layer slice Sn_max to A;
for k = n_max -1 to 0
    j_max ← the total number of polygons in S_k;
    foreach a_i of A and polygon S_k^j do
        if (all a_i are not inside the polygon S_k^j) then //INOUT(A, S_k) = 0
            Add Centroid of S_k^j to A;
        end
    end
end
```

The 3D shape of the robot is roughly constructed using the assembly strings that are geometrically generated as above. In practice, the robot is locally deformed or distorted because the vertical compliances of the folded hinges are not symmetrical around the string holes. This issue is lessened if additional assembly strings are added to counter-balance the elastic forces of hinges. For example, the main body of the bunny robot has two assembly strings *a* and *b* which are generated based on the geometrical condition. By the user's request and settings, however, one more string *c* is generated next to the string *b* (Fig. 4(b)). Adjusting the preloading forces of the strings *a*, *b*, and *c* that make a triangular formation, we can modulate the initial 3D shape of the assembled robot. After the 3D assembly, the robot's local motions are controlled by selectively modulating the assembly strings.

After designing the structure of the robot, we estimate its motions using a mechanical model. Because the weight of the main material (polyester film) is light-weight and highly elastic, we assume that the robot is a low mass system with multiple springs. The behavior of the model is governed by

$$\mathbf{K}\mathbf{Z} = \Delta\mathbf{F} \tag{5}$$

where **Z** is the height changes of critical points in Fig. 5(a), **K** is a diagonal matrix about the spring constants, and **F** is the tensional forces applied to the strings. Fig. 5(a) shows a simplified mechanical model. The green, purple, and red planes present several layers shared by strings, indicating the head, back and bottom parts respectively. Using the position and orientation of these planes, we can estimate the workspace, behavior and the string forces to maintain the robot shape. We simulate the robot's motion using the stiffness and the desired heights from the 3D model (Fig. 5(b)-(e)). The four flexible strings pull the four parts of the bunny robot from under the base. As a result, the bunny robot shrinks its body, turns its head leftwards, and stretches its body, respectively. Table 1 presents the summarized simulation parameters and results.

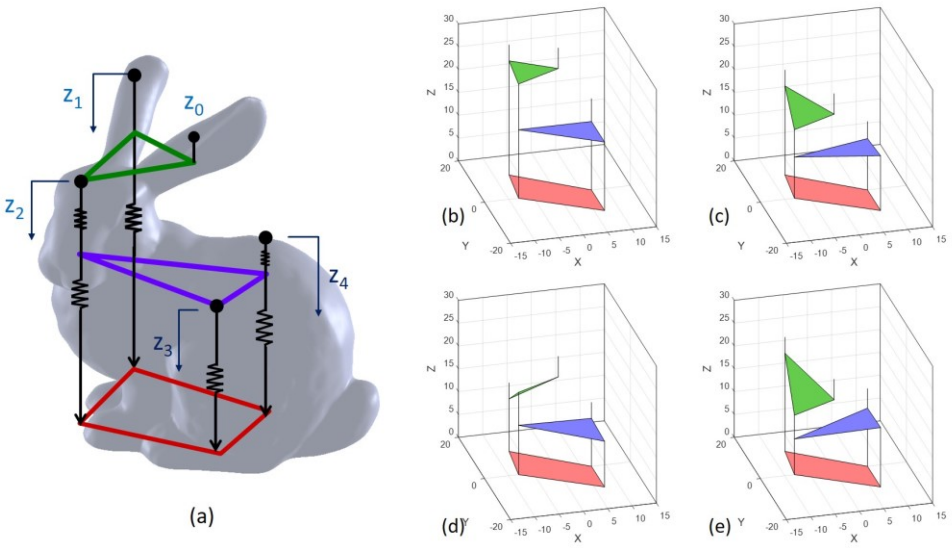

Fig. 5. (a) The simplified mechanical model of the soft bunny robot consisting of multiple springs. (b)-(e) Simulation motions on the bunny robot's local actuation.

Table 1. The motions of the bunny robot and simulated string forces for Fig. 5(c)-(e)

	(c) $Z = [-5.5\ -10\ -3\ -5]^T$	(d) $Z = [-13.5\ -7\ -5\ -6]^T$	(e) $Z = [-3.5\ -12\ -2\ -3]^T$
ΔF(N)	0.27	0.67	0.17
	2.30	1.60	2.80
	0.90	1.50	0.60
	1.36	1.60	0.92
Assumption: Stiffness $[k_1\ k_2\ k_3\ k_4] = [0.05\ 0.86\ 0.30\ 2.0]^T$ (N/mm)			

ii) *Global Actuation Strings*: In order to change the global position and orientation of the robot, maximum three strings are connected with the bottom layer. The bunny robot has three string holes (H_d, H_e, and H_h in Fig. 6) on the same line, which are pulled from the base holes (Q_d, Q_e, and Q_f in Fig. 6) by the strings *d*, *e*, and *h* (Fig 4). Modulating the lengths of these strings, users rotate and translate the robot within in the triangular area formed by Q_d, Q_e, and Q_f where the robot's 2D position and orientation are coupled (Fig. 7).

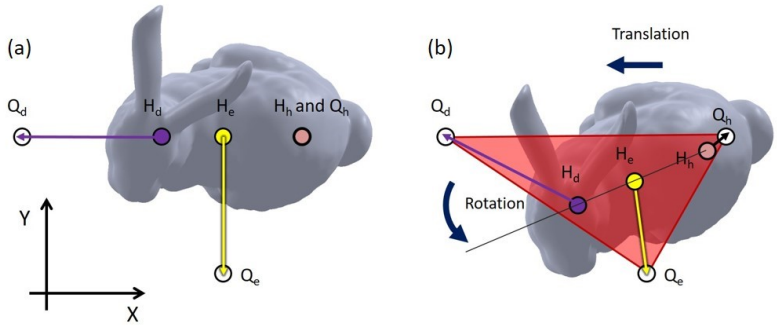

Fig. 6. (a) The bunny robot has three string holes H_d, H_e, and H_h at the bottom layer, which are pulled from the base holes Q_d, Q_e, and Q_h. (b) The lengths of the global actuation strings d, e, and h determine the position and orientation of the bunny robot.

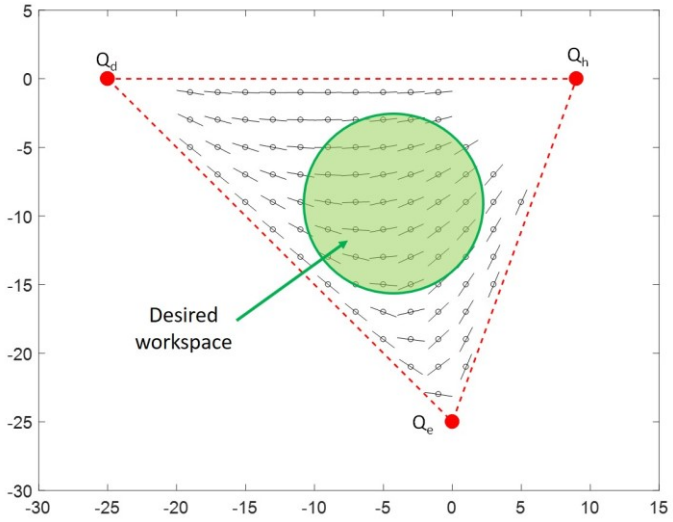

Fig. 7. Simulated workspace of the bunny robot. The small circles and arrows indicate the numerically calculated position and orientation of the point H_e at the center of the bunny robot to satisfy two kinematic equilibrium equations: $\sum F = 0$, and $\sum M = 0$. We locate Q_d, Q_e, and Q_h to include the desired workspace in the triangular area.

3. Fabrication by Additive Folding

The main material used for the bunny robot is 100 μm thick polyester film (Dura-lar film, Grafix), which is lightweight, dimensionally stable, highly elastic and resistive to tearing. Using a desktop automatic paper-crafting machine (Silhouette CAMEO, Silhouette America), we manufacture flexible strips of the fold patterns including 2D slices, foldable hinges, and string holes, and then manually thread the nylon strings up and down through the holes (Fig. 8(a)). The base platform on which the robot stands and is anchored has arrays of grid holes (13 row, 13 column, 2.5 mm distance between grids), and is 3D-printed. After penetrating the base layer, all strings go into grid holes of the base platform. If the strings are pulled, the slices are successively layered from the base as in additive manufacturing (Fig. 8(b)-(d)). The strings are pulled until the height of the model reaches the desired value, and finally fixed at the banister of the platform. If the strings are fixed, the elastic restoring forces of folded hinges pull the strings, and the preloading forces maintain the shape of the fabricated robot.

The working principle of the additive folding mechanism is depicted in Fig. 9. If the pulling force F_1 is stronger than the sum of the friction between the string and hole (in L_1) and the elastic restoring force of the hinge, the string slides along the hole and the layer L_2 starts to be folded. By the moment-force relation, the rotational angle θ_1 is calculated using

$$F_2 = F_1 - f_1(\theta_1) = \frac{\kappa\theta_1}{r_1\left(\sin\frac{\theta_1}{2}\right)} \tag{6}$$

where κ is the torque constant (i.e., rotational stiffness) of the elastic hinge about the rotational angle, and f_1 is the friction between the hole at the layer L_1 and the string. Considering the friction is caused by the edge of the string hole, we assume the profile of friction force as

$$f_1(\theta_1) = f_{max}\cos(\frac{\theta_1}{2}) \tag{7}$$

where $0 < \theta < \theta_{max}$. This model shows that the friction is maximized when L_1 and L_2 are flat (i.e., $\theta_1 = 0$) while it is minimized when the string is normal to the surface (i.e., $\theta_1 = \pi$).

We simulate the folding process of three layers, and investigate numerical value of each force under some assumptions: f_{max} is 0.5N, κ is 0.5N·mm/rad and θ_{max} =175 deg. As shown in Fig. 9(c) and (d), L_2 starts to be folded as F_1 becomes 0.60N. The layer's folding is accelerated because the friction becomes smaller as the folding angle θ_1 increases. At the final state (*i.e.*, fully folded, θ =175 deg.), the friction between the string and L_1 is about 0.02N. The rest 0.58N becomes F_2, sustaining the folded L_2 and pulling the next layer L_3. L_3 is not folded until F_2 reaches 0.60N. If F_1 increases more and F_1 becomes beyond that value, L_3 starts to be abruptly folded as L_2. This folding process continues to propagate as the slices are layered down. Fig. 10 shows a simulation of how 30 slices fold into a cylinder shape.

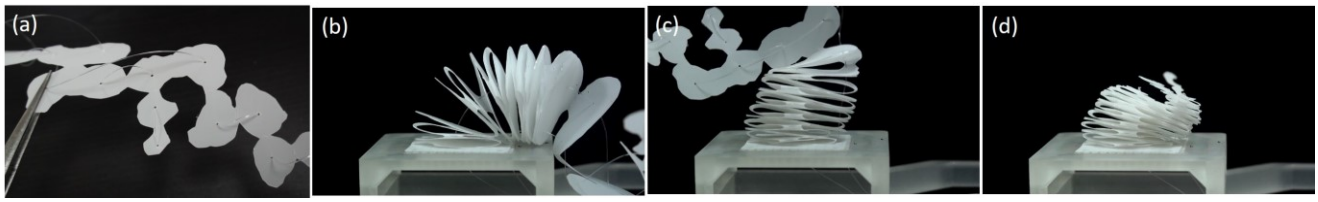

Fig. 8. Fabrication by additive folding. (a) Slices threaded by strings. (b)-(d) Snapshots of the articulated slices which fold to reconstruct the bunny model. The balanced shape is finally made by modulating the assembly strings.

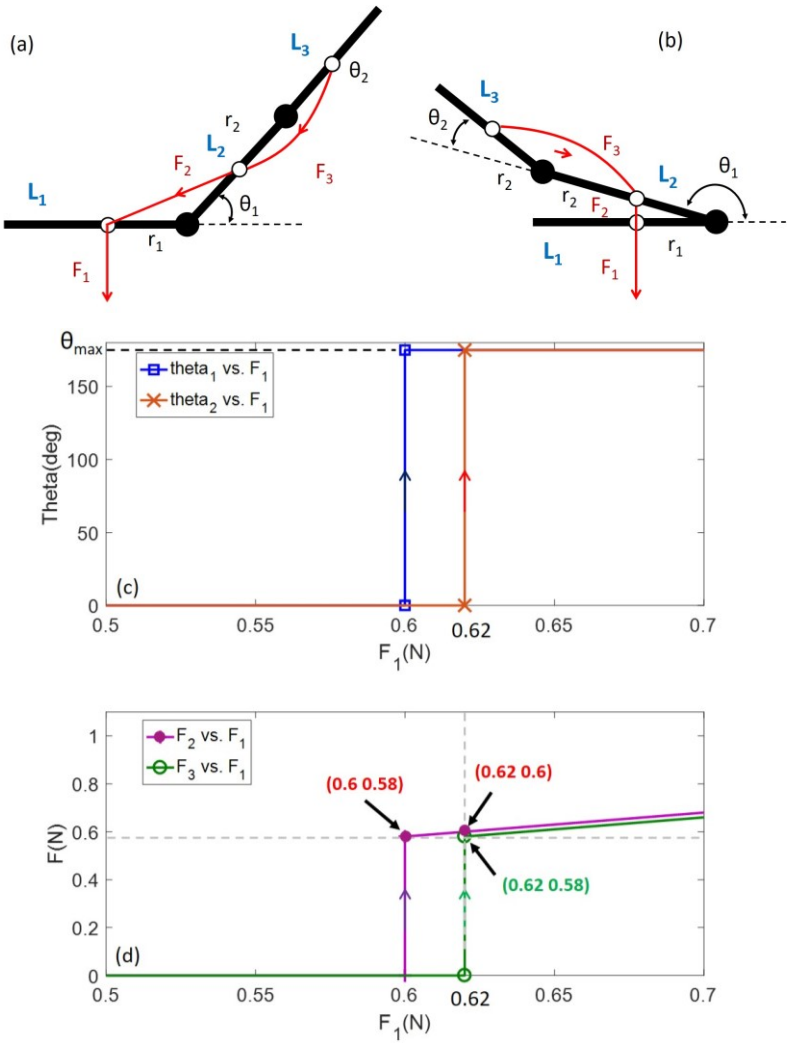

Fig. 9. The free-body-diagram and simulation results of the additive folding mechanism. The strip has three articulated slices. (a) L_2 starts to be folded when F_1 becomes stronger than the sum of the initial friction and the elastic restoring force of the hinge. (b) If F_1 continues to increase after fully folding L_2, F_2 also increases accordingly and fold L_3 when F_2 is 0.60N (*i.e.*, F_1 is 0.62N). (c) and (d) show the rotational angles (as a function of F_1) and F_2 and F_3 (as a function of F_1), respectively.

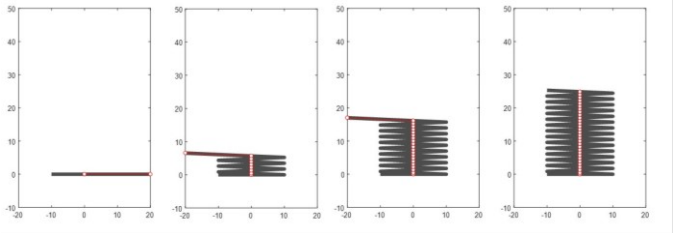

Fig. 10. Simulated additive folding of a strip (n = 30) to a cylinder.

4. PHYSICAL ANIMATION

Animation is the act of generating movement by manipulating the folded 3D structure using the embedded strings. Technically, pulling the strings causes the connected parts to contract or move, resulting in local changes of the robot body. During these motions, the restoring forces in the folds balance out, making the deformations look smooth. If the strings are relaxed, the original shape of the robot is instantly recovered by the elastic restoring forces of the folds.

The bunny model is an example of a complex nonconvex geometry that can be fabricated using additive folding. The fold pattern for this structure demonstrates not only the basic method of slice attachment described, but also multiple hinge attachments added for multi-piece slices and nonconvex slices. We can actuate all or a subset of the slices of the structure using strings (Fig.11 and multimedia extension 2). As estimated in the motion design and simulation stage, the bunny's head, central back and left back are compressed or released by the strings *a, b* and *c*, respectively. These combinations control the robot's pose and shape. The string *f* causes the symbol of the bunny robot, the right ear, to flinch or wag. The strings *d*, *e*, and *h* allow the rotation of the front body and the translation of the whole body. If the local actuation and global strings are combined, the aforementioned motions are implemented at different 2D positions.

From a bio-inspired design perspective, the strings are flexible skeletons and artificial muscles for animating the robot, and the folded slices perform the roles of fleshes and skins to form the appearance. Articulated layers are automatically distributed along strings, and reoriented by applied tensions. The layers behave harmoniously as if a single soft body and subordinate limbs move. As a result, the motions of the animatronic robot are soft and natural as musculoskeletal systems. In addition to the presented motions, we could realize different motions such as breathing and wiggling by pulling the embedded strings with a time delay. Another reason of the life-like motions is the elasticity intrinsic to the folded robots. Technically, the folded bunny is a low mass inertia system connected with multiple vertical springs (Fig. 5).

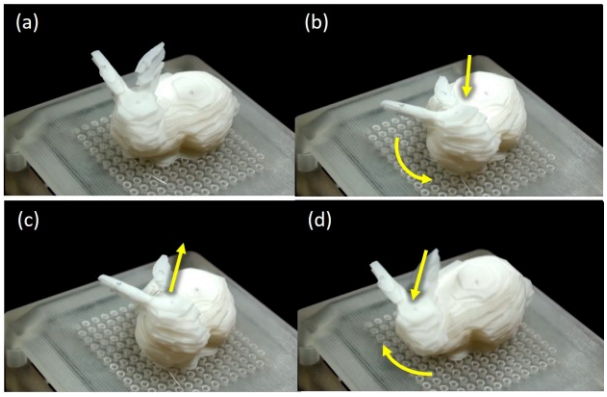

Fig. 11 Physical animation of the soft bunny robot. (a) The idle state of the bunny robot. The yellow arrows indicate (b) the rotation and compression of the front body, (c) the relaxed head and front body, and (d) the compressed head and the moving direction. See the multimedia extension 2.

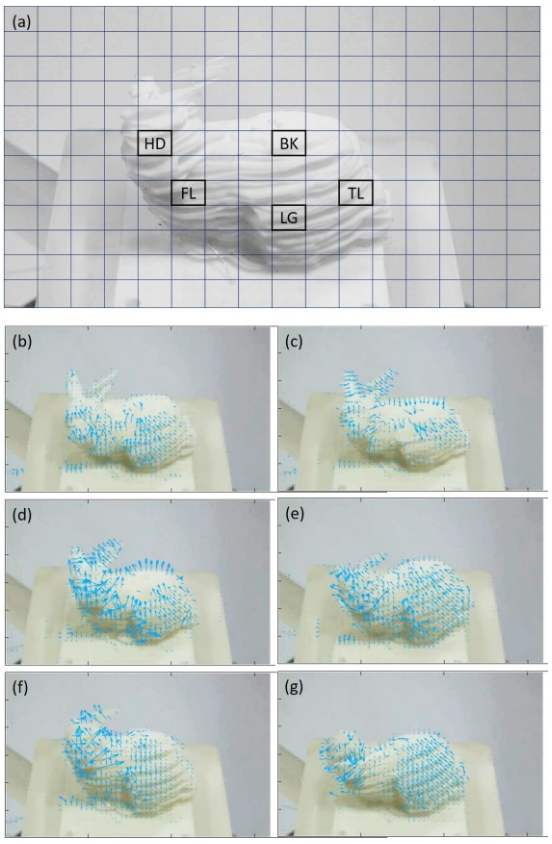

Fig. 12 Optical flows on the bunny robot. (a) HD, BK, LG, TL, and FL indicate the pixel locations of the head, back, leg, tail, and low-front body. The arrows indicate the region of the high velocity such as (b) the head and leg (t =2.4 sec), (c) the ears, head, and back (t =2.5 sec), (d) the two ears, front body and leg (t = 2.5 sec), (e) the entire body (t = 4.1 sec), (f) the two ears and front body (t = 5.7 sec), and (g) the head and rear body (t = 13.7 sec), respectively. See the multimedia extension 3.

Table 2. Correlation coefficients between local optical flows in Fig. 12(b)-(g)

(b)	HD	BK	LG	TL	FL
HD	1.0	0.30	-0.19	0.19	0.34
BK	0.30	1	0.04	0.08	0.00
LG	-0.19	0.04	1	0.67	0.49
TL	0.19	0.08	0.67	1	0.14
FL	0.34	0.00	0.49	0.14	1

(c)	HD	BK	LG	TL	FL
HD	1	0.85	0.82	0.68	0.78
BK	0.85	1	0.77	0.71	0.67
LG	0.82	0.77	1	0.81	0.88
TL	0.68	0.71	0.81	1	0.49
FL	0.78	0.67	0.88	0.49	1

(d)	HD	BK	LG	TL	FL
HD	1	0.79	0.81	0.81	0.90
BK	0.79	1	0.89	0.82	0.55
LG	0.81	0.89	1	0.91	0.74
TL	0.81	0.82	0.91	1	0.71
FL	0.90	0.55	0.74	0.71	1

(e)	HD	BK	LG	TL	FL
HD	1	-0.02	0.47	0.78	-0.56
BK	-0.02	1	0.65	0.17	0.40
LG	0.47	0.65	1	0.75	0.00
TL	0.78	0.17	0.75	1	-0.34
FL	-0.56	0.40	0.00	-0.34	1

(f)	HD	BK	LG	TL	FL
HD	1	0.88	0.86	0.79	0.94
BK	0.88	1	0.83	0.69	0.88
LG	0.86	0.83	1	0.86	0.85
TL	0.79	0.69	0.86	1	0.86
FL	0.94	0.88	0.85	0.86	1

(g)	HD	BK	LG	TL	FL
HD	1	0.74	-0.05	0.26	0.33
BK	0.74	1	0.06	0.35	0.31
LG	-0.05	0.06	1	0.46	0.46
TL	0.26	0.35	0.46	1	0.72
FL	0.33	0.31	0.46	0.72	1

The delicate motion of the soft bunny robot are visualized using optical flow techniques (Fig.12 and multimedia extension 1). The arrows indicate the region of high velocity in 2D images. Using the correlation coefficients of optical flows at different regions, we can quantify the degree to which the movements of each part are associated (Fig. 12(a)). HD, BK, LG, TL, and FL indicate the pixel locations of the head, back, leg, tail, and low-front body, respectively. Fig. 12(b)-(g) and Table 2 show the processed images and summarized correlation coefficients. The bunny robot shows different combinations of local actuation. Therefore, the correlation coefficients between the same two parts could be high (HD-BK: 0.85 in Table 2(c) and 0.88 in (f)) or low (HD-BK: 0.3 in Table 2(b) and -0.02 in (e)).

We investigate if the demonstrated animatronic motions are implementable in different size robots. Because bandwidth is an objective metric to determine the dynamic response of a mechanical system, we calculated the bandwidth index $(k/m)^{0.5}$ of different sizes of bunny robots (e.g., 25mm – 50mm), measuring the weight and the vertical stiffness. The result show the bandwidth index is inversely proportional to the length scale of the robot (Fig. 13), which is consistent with the scaling law. That means, in order to employ additive folding to make larger robots, thicker materials need to be used. Otherwise, the robot is limp, and moves slowly when animated.

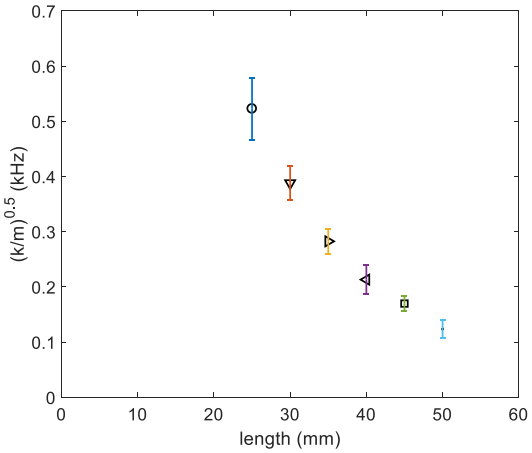

Fig. 13 The experimentally measured bandwidth index as a function of the robot size (i.e., the maximum length of a slice). Multiple bunny robots are made by scaling the original bunny robot (length: 35 mm) up and down. The weight m and stiffness k are experimentally measured, and the bandwidth index $(k/m)^{0.5}$ are calculated.

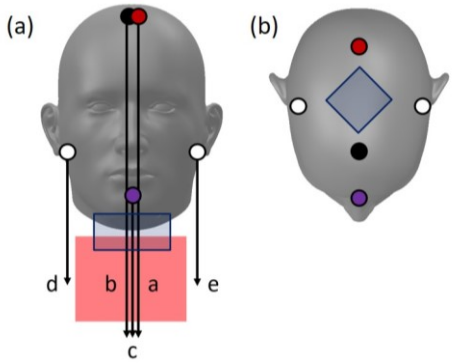

Fig. 14 (a) The front-view and (b) the top-view show five strings connected to the top layers, two ears, and the chin of the animatronic human head model. By pulling these strings, the human head nods, tilts in two directions, and talks. The navy-colored boxes show that the head part is connected to the neck part via four strings for the shaking motion. The applied mechanism is detailed in Appendix 2.

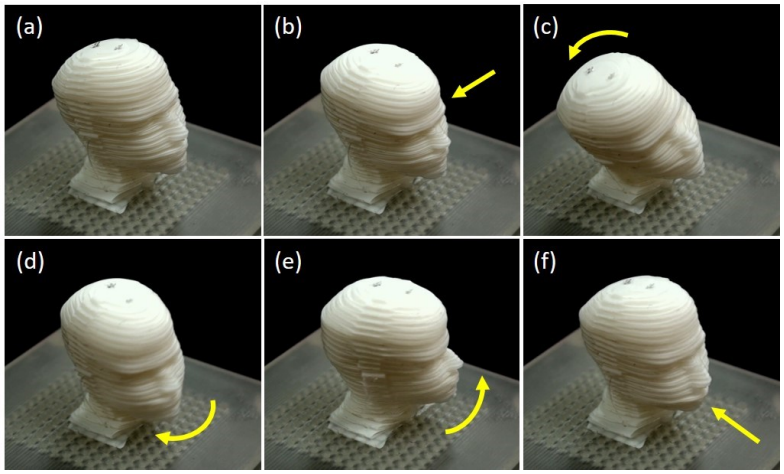

Fig. 15. The animatronic human head's motions actuated by strings. (a) Idle state of the robot, (b) glaring eyes, (c) tilting the head right left, (d) and (e) turning the head left and right, (f) talking. See the multimedia extension 4.

5. Advanced Applications: Audio-animatronics

Audio-animatronics is the advanced application of the developed robots. Their soft and natural motions are synchronized with vocal sounds, which significantly enhances audio-visual interaction between the robots and humans. This section introduces an animatronic human head (Fig. 14 and Fig. 15) created by the end-to-end implementation method and a case-study for its applications. In order to enhance the resolution embodied by a nose, eyes, mouth, chin, cheeks and neck, we generate a one-row fold pattern having 50 slices where hinges are located at the two sides of the model. The slices are threaded by 9 strings and assembled into the 3D model by additive folding. In the idle state, the head's detailed facial parts including the forehead, eyebrows, nose, cheeks, chin, and neck are clearly visible (Fig. 15(a)). The strings can be used to perform local motions such as contracting the forehead, nodding, tiling, and even shaking the head, or expanding the mouth area. This set of movements enables expressive animations that simulate anger (Fig. 15(b)), confusion (Fig. 15(c)), denying (Fig. 15(d) and (e)), talking (Fig. 15(f)), and other common gestures. These string-driven motions produce a very unique sensation to observers because folded slices move similarly to soft flesh, and because its motion transition is compliant.

We synchronize the local motions of the robotic head with an audio material (one-minute length monologue from a movie "*Life of Pi*") as if the robot were talking. The multimedia extension 2 shows the head, eye, and mouth are individually activated, and that such facial motions are composed into more complex ones. The robot's talking motion actuated by the strings is more delicate than the gestures in Fig. 15 because the motion range is small (< 3mm). We set six locations representing the forehead, left eye, right eye, cheek, nose, and mouth (Fig. 16), and calculated the correlations of optical flows at the parts in all images (1577 frames). Table 2 shows that the movements of the two eyes, the right eye and nose, and the nose and mouth are strongly correlated (> 0.8). The cheek is relatively uncorrelated to the left eye and forehead (0.72 and 0.67). The most distant two parts, the forehead and the mouth also shows relatively weak correlation. The mouth's movement affects the nose's one because their locations are close.

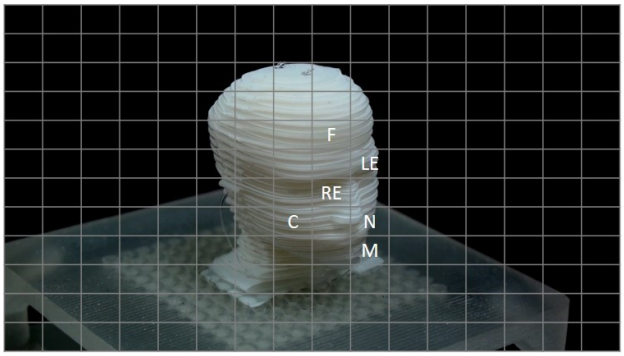

Fig. 16 Audio-animatronic experiments. The animatronic human head in the segmented image. F, RE, LE, C, N and M indicate the pixel locations of the forehead, right eye, left eye, cheek, nose and mouth. See the multimedia extension 5.

Table 3. The average correlation coefficients of local optical flows (total: 1577 frames)

	F	LE	RE	N	M	C
F	1	0.88	0.71	0.72	0.73	0.67
LE	0.88	1	0.88	0.79	0.76	0.72
RE	0.71	0.88	1	0.93	0.88	0.88
N	0.72	0.79	0.93	1	0.98	0.93
M	0.73	0.76	0.88	0.98	1	0.93
C	0.67	0.72	0.88	0.93	0.93	1

6. Discussion

Additive folding inspired by 3D printing is a new type of fabrication mechanism that also enables soft actuation of animatronic robots employing embedded flexible strings. In this paper, we have presented the end-to-end design, fabrication and animation process, but there are several limitations intrinsic to structures and improvements to be further investigated for extensive applications.

(*i*) *Resolution*: the fabrication resolution is limited due to the gap distance between layers, and the minimum size of fabricable slices. Compared to the actual bunny model, for example, the ears of the fabricated are blunt and flat because the top layers are too small (< 2mm-by-2mm) to manufacture with a paper-crafting machine. In the case of the human head model, the ears were lost in the hinges at the two sides. One practical solution to alleviate this issue is increasing the model size. We can minimize the number of discarded layers and build small hinges compared with the overall size of the model, which expresses delicate geometries with an enhanced resolution.

(ii) *Scalability*: The experimental models that we have demonstrated are on the order of tens to hundreds of millimeters in size. Larger models can be fabricated using a roll-type polyester film, which is available off-the-shelf, and the corresponding mode of the cutting machine. Another important design consideration is that the actual stiffness of the robot changes along with its dimension. According to scaling laws, the bending stiffness of a slice (or a hinge) to form a twice bigger object becomes only about 6% of the original one if not a thicker material is used. In our case, we concluded that the material thickness should be at least 0.4 mm to be used for models of 150 mm length.

(*iii*) *Automated fabrication*: the build times for the animatronic bunny and human head are about 60 minutes and 70 minutes, respectively. In all cases, routing the layers with strings consumes a high portion (40 minutes and 50 minutes). To fully automate the fabrication process, this manual folding needs to be replaced with machines such as a computer-controlled sewing machine or a desktop computer numerical control (CNC) platform. Also, thermally or magnetically activated self-folding mechanism of multi-layered smart composite materials could be employed (Sung et al., 2017; Yim et al., 2014; Yim et al., 2014; Miyashita et al., 2015).

7. Conclusion

In this paper, we focus on introducing the overall implementation process and unprecedented demonstrations of *animatronic soft robots by additive folding*, highlighting that computational design, rapid fabrication, and soft actuation are serially connected. In particular, this new approach enables the creation of animatable robotic system whose movement is inspired by the musculoskeletal creatures, using the embedded flexible strings and the deflection of slices, because the harmonious motions of the individual slices produce a unique visual effect. In this sense, the 3D fabrication by additive folding will open a new approach towards *soft robots* and *animatronics* (Shepherd et al., 2011; Brown et al., 2010; Terada et al., 2004; Rus et al., 2015). Future works include integration of various printable sensors and electric motor-based actuation system for feedback-control, as depicted in Fig. 2.

Funding

This work was supported by Korea Institute of Science and Technology (KIST) and National Science Foundation (NSF) grants numbers 1240383 and 1138967.

REFERENCES

Bartlett NW, Tolley MT, Overvelde JT, Weaver JC, Mosadegh B, Bertoldi K, Whitesides GM and Wood RJ (2015) A 3D-printed, functionally graded soft robot powered by combustion. *Science*, *349*(6244), pp.161-165.

Brown E, Rodenberg N, Amend J, Mozeika A, Steltz E, Zakin MR, Lipson H and Jaeger HM (2010) Universal robotic gripper based on the jamming of granular material. *Proceedings of the National Academy of Sciences*, *107*(44), pp.18809-18814.

Cesaretti G, Dini E, De Kestelier X, Colla V and Pambaguian L (2014) Building components for an outpost on the Lunar soil by means of a novel 3D printing technology. *Acta Astronautica*, *93*, pp.430-450.

Dawood A, Marti BM, Sauret-Jackson V and Darwood A (2015) 3D printing in dentistry. *British dental journal*, *219*(11), pp.521-529.

Davison N (2015) 3D-Printed Cities: Is This the Future?. *The Guardian*, *26*, p.2015.

Eckel ZC, Zhou C, Martin JH, Jacobsen AJ, Carter WB and Schaedler TA (2016) Additive manufacturing of polymer-derived ceramics. *Science*, *351*(6268), pp.58-62.

Espalin D, Muse DW, MacDonald E and Wicker RB (2014) 3D Printing multifunctionality: structures with electronics. *The International Journal of Advanced Manufacturing Technology*, *72*(5-8), pp.963-978.

Gibson I, Rosen DW, Stucker B (2010) *Additive manufacturing technologies* (vol. 238), New York: Springer.

Goldstein SC, Campbell JD and Mowry TC (2005) Programmable matter. *Computer* **38**, pp. 99-101.

Hawkes E, An B, Benbernou NM, Tanaka H, Kim S, Demaine ED, Rus D and Wood RJ (2010) Programmable matter by folding. *Proceedings of the National Academy of Sciences*, *107*(28), pp.12441-12445.

Jung JW, Lee JS and Cho DW (2016) Computer-aided multiple-head 3D printing system for printing of heterogeneous organ/tissue constructs. *Scientific reports*, *6*.

Kang HW, Lee SJ, Ko IK, Kengla C, Yoo JJ and Atala A (2016) A 3D bioprinting system to produce human-scale tissue constructs with structural integrity. *Nature biotechnology*, *34*(3), pp.312-319.

Kim SH, Choi KH, Cho SJ, Choi S, Park S and Lee SY (2015) Printable solid-state lithium-ion batteries: a new route toward shape-conformable power sources with aesthetic versatility for flexible electronics. *Nano letters*, *15*(8), pp.5168-5177.

Lipson H and Melba K (2013) Fabricated: the new world of 3D printing. John Wiley & Sons.

MacCurdy R, Katzschmann R, Kim Y and Rus D (2016) Printable hydraulics: a method for fabricating robots by 3D co-printing solids and liquids. In *Proceedings of the IEEE International Conference on Robotics and Automation,* pp. 3878-3885.

Micallef J (2015) What's Possible with 3D Printing?. In *Beginning design for 3D printing*.pp. 1-30. Apress.

Miyashita S, Guitron S, Ludersdorfer M, Sung CR, and Rus D (2015) An untethered miniature origami robot that self-folds, walks, swims, and degrades. In Proc. of the IEEE International Conference on Robotics and Automation, pp. 1490–1496.

Morrison RJ, Hollister SJ, Niedner MF, Mahani MG, Park AH, Mehta DK, Ohye RG. and Green GE (2015) Mitigation of tracheobronchomalacia with 3D-printed personalized medical devices in pediatric patients. *Science translational medicine*, *7*(285), pp.285ra64-285ra64.

Murphy SV and Atala A (2014) 3D bioprinting of tissues and organs. *Nature biotechnology*, *32*(8), pp.773-785.

Muth JT, Vogt DM, Truby RL, Mengüç Y, Kolesky DB, Wood RJ and Lewis JA (2014) Embedded 3D printing of strain sensors within highly stretchable elastomers. *Advanced Materials*, *26*(36), pp.6307-6312.

Müller A, Krishnan KG, Uhl E and Mast G (2003) The application of rapid prototyping techniques in cranial reconstruction and preoperative planning in neurosurgery. *Journal of Craniofacial Surgery*, *14*(6), pp.899-914.

Peng H, Mankoff J, Hudson SE and McCann J (2015) A layered fabric 3D printer for soft interactive objects. In: *Proceedings of the Annual ACM Conference on Human Factors in Computing Systems*, pp. 1789-1798.

Perkins I and Skitmore M (2015) Three-dimensional printing in the construction industry: A review. *International Journal of Construction Management*, *15*(1), pp.1-9.

Poukens J, Haex J and Riediger D (2003) The use of rapid prototyping in the preoperative planning of distraction osteogenesis of the cranio-maxillofacial skeleton. *Computer Aided Surgery* 8(3), pp.146–154.

Ribeiro F (1998) 3d printing with metals. *Computing & Control Engineering Journal*, *9*(1), pp.31-38.

Rus D, Tolley MT (2015) Design, fabrication and control of soft robots. *Nature* 521(7553), pp. 467-475.

Sun K, Wei TS, Ahn BY, Seo JY, Dillon SJ and Lewis JA (2013) 3D printing of interdigitated Li-Ion microbattery architectures. *Advanced Materials*, *25*(33), pp.4539-4543.

Sung CR, Lin R, Miyashita S, Yim S, Kim S, and Rus D (2017) Self-folded Soft Robotic Structures with Controllable Joints, In *Proceedings of the IEEE International Conference on Robotics and Automation,* to appear.

Shepherd RF, Ilievski F, Choi W, Morin SA, Stokes AA, Mazzeo AD, Chen X, Wang M and Whitesides GM (2011) Multigait soft robot. *Proceedings of the National Academy of Sciences*, *108*(51), pp.20400-20403.

Terada Y and Yamamoto I (2004) An animatronic system including lifelike robotic fish. *Proceedings of the IEEE*, *92*(11), pp.1814-1820.

Tumbleston, JR, Shirvanyants D, Ermoshkin N, Janusziewicz R, Johnson AR, Kelly D, Chen K, Pinschmidt R, Rolland JP, Ermoshkin A and Samulski ET (2015) Continuous liquid interface production of 3D objects. *Science*, *347*(6228), pp.1349-1352.

Wang G, Yao L, Wang W, Ou J, Cheng CY and Ishii H (2016) xPrint: A Modularized Liquid Printer for Smart Materials Deposition. In *Proceedings of the Annual ACM Conference on Human Factors in Computing Systems*, pp. 5743-5752.

Yim S, Gultepe E, Gracias DH and Sitti M (2014) Biopsy using a magnetic capsule endoscope carrying, releasing, and retrieving untethered microgrippers. *IEEE Transactions on Biomedical Engineering*, *61*(2), pp.513-521.

Yim S and Sitti M (2014) SoftCubes: Stretchable and self-assembling three-dimensional soft modular matter. *The International Journal of Robotics Research*, *33*(8), pp.1083-1097.

Yokota T, Inoue Y, Terakawa Y, Reeder J, Kaltenbrunner M, Ware T, Yang K, Mabuchi K, Murakawa T, Sekino M and Voit W (2015) Ultraflexible, large-area, physiological temperature sensors for multipoint measurements. *Proceedings of the National Academy of Sciences*, *112*(47), pp.14533-14538.

Appendix 1

Table of Multimedia Extension

Extension	Media type	Description
1	Video	The end-to-end implementation process of animatronic soft robots (Fig. 2)
2	Video	Experimental demonstration of the bunny robot (Fig. 11)
3	Video	Optical flow of the bunny robot (Fig. 12)
4	Video	Experimental demonstration of the gesturing animatronic human head robot (Fig. 15)
5	Video	Experimental demonstration of the human head robot moving according to an audio clip (Fig. 16). Note that audio is removed because of the copyright.

Appendix 2 Rotating the robotic head about the vertical axis

Fig. 17 shows the mechanism used for the shaking motion of the human head robot. The two parts corresponding the head and the neck are connected by only strings. If the strings *g* and *h* are pulled, their string holes at the bottom layer of the head part are pulled and overlapped onto the string holes of the top layer of the neck part. As a result, the head part is rotated in the counterclockwise direction. If the other strings are pulled, the head is rotated in the opposite direction

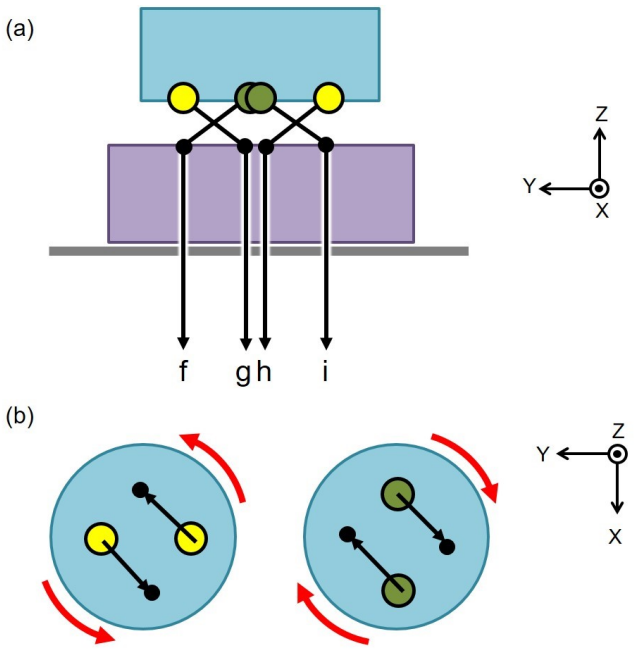

Fig. 17 (a) The front-view and (b) the top-view show four strings connected to the bottom layer of the upper part. Note that the upper and lower parts are connected by strings, not hinges. We can rotate only the upper part (blue) in both directions using the strings *g* and *h* (or *f* and *i*), counter-clockwise (or clockwise).